The Astrophysical Journal Letters, 986:L34 (15pp), 2025 June 20 https://doi.org/10.3847/2041-8213/add536

A Heavy-metal Scenario of Ultra-high-energy Cosmic Rays

Jakub Vícha[1], Alena Bakalová[1], Ana L. Müller[1], Olena Tkachenko[1], and Maximilian K. Stadelmaier[2,3]
[1] Institute of Physics of the Czech Academy of Sciences, Prague, Czech Republic; vicha@fzu.cz
[2] Università degli Studi di Milano, Dipartimento di Fisica & INFN, Sezione di Milano, Milano, Italy
[3] Karlsruhe Institute of Technology, Institut für Astroteilchenphysik, Karlsruhe, Germany
Received 2025 April 15; revised 2025 May 6; accepted 2025 May 7; published 2025 June 19

Abstract

The mass composition of ultra-high-energy cosmic rays is an open problem in astroparticle physics. It is usually inferred from the depth of the shower maximum ($X_{\rm max}$) of cosmic-ray showers, which is only ambiguously determined by modern hadronic interaction models. We examine a data-driven scenario, in which we consider the expectation value of $X_{\rm max}$ as a free parameter. We test the novel hypothesis of whether the cosmic-ray data from the Pierre Auger Observatory can be interpreted in a consistent picture, under the assumption that the mass composition of cosmic rays at the highest energies is dominated by high metallicity, resulting in pure iron nuclei at energies above ≈40 EeV. We investigate the implications on astrophysical observations and hadronic interactions, and we discuss the global consistency of the data assuming this heavy-metal scenario. We conclude that the data from the Pierre Auger Observatory can be interpreted consistently if the expectation values for $X_{\rm max}$ from modern hadronic interaction models are shifted to larger values.

Unified Astronomy Thesaurus concepts: Ultra-high-energy cosmic radiation (1733); Nuclear abundances (1128); Spectral energy distribution (2129); Cosmic ray showers (327)

1. Introduction

The mass composition of ultra-high-energy cosmic rays (above 10^{18} eV) is an important puzzle piece concerning the question of the origin of the most energetic particles in the Universe. These rare particles produce extensive air showers of secondary particles that are detected by large observatories, such as the Pierre Auger Observatory (A. Aab et al. 2015a) and Telescope Array (T. Abu-Zayyad et al. 2012). The observables that are the most commonly used as mass estimators of the primary cosmic-ray particles are the depth of the shower maximum ($X_{\rm max}$) and the number of muons produced during the development of the air shower and reaching the ground. The value of $X_{\rm max}$ is measured from the top of the atmosphere in units of g cm^{-2} and indicates where the air shower reaches its maximum particle count.

Another important observable in the context of air-shower development is the number of muons created in the cascade. An accurate estimate of the number of muons that reach the ground is very difficult to achieve using modern air-shower models; this pathology is known as the muon problem (J. Albrecht et al. 2022). The state-of-the-art hadronic interaction models do not agree on the average $X_{\rm max}$ or on the number of hadronic shower particles (pions, muons, etc.) produced in air showers of the same type of primary particle and primary energy. These model disagreements are a consequence of conceptual differences in extrapolations of hadronic interaction properties studied at much lower energies and different kinematic regions using human-made accelerators. However, these models produce consistent and stable expectations for fluctuations in both observables (A. Aab et al. 2021).

With the advent of novel machine learning techniques being applied to the Pierre Auger Observatory (Auger) Surface Detector data (A. Abdul Halim et al. 2025a, 2025b), an unprecedentedly precise estimation of the mean and fluctuation of $X_{\rm max}$ was recently achieved for primary energies ranging from 3 EeV up to 100 EeV. However, the resulting moments of the logarithmic atomic mass number ($\ln A$) cannot be consistently interpreted using modern hadronic interaction models. In the case of the QGSJET II-04 (S. Ostapchenko 2011) model of hadronic interactions, a negative and thus nonphysical variance of logarithmic atomic mass $\ln A$, $\sigma^2(\ln A)$, is obtained even when accounting for systematic uncertainties. In the case of the SIBYLL 2.3d (F. Riehn et al. 2020) and EPOS-LHC (T. Pierog et al. 2015) models, the predictions lie at the edge of the systematic uncertainty range of the data. The variance $\sigma^2(\ln A) \approx 0$ suggests a pure beam of primary cosmic rays above $E \simeq 5$ EeV (within uncertainties), while the energy evolution of the average $X_{\rm max}$ is only consistent with a gradual increase in the average logarithmic mass $\langle \ln A \rangle$ as a function of the primary energy. These inconsistencies could be resolved for all three models if the $X_{\rm max}$ scale of models is shifted toward deeper values for the same primary particles.

Recently, fits of two-dimensional distributions of the ground signal and $X_{\rm max}$ in the energy range 3–10 EeV have revealed an alleviation of the muon problem (A. Abdul Halim et al. 2024a), reducing it by approximately half compared to the previous analyses in A. Aab et al. (2015b, 2016a, 2020a). To match the two-dimensional distributions with a consistent interpretation of the mass composition, the expected scale of the number of hadronic shower particles needs to be increased by ≈15%–25%. At the same time, the simulated average $X_{\rm max}$ from all three aforementioned models tends to be shifted independently of the primary mass by ≈20–50 g cm^{-2}, implicitly, for a heavier mass composition than for the unmodified model predictions. Such primary-mass independent shifts of the predicted $X_{\rm max}$ scale could be qualitatively

explained by a change in the normalization of the energy evolution of elasticity or multiplicity in hadronic interactions (A. Abdul Halim et al. 2024a).

The $X_{\rm max}$ fluctuations produced for simulated showers from iron nuclei are too low using the EPOS-LHC model, being at the level of total defragmentation of the Fe nucleus. This issue will be resolved in the upcoming model version EPOS-LHCR (T. Pierog & K. Werner 2023), which will produce $X_{\rm max}$ fluctuations at the level of expectations from the QGSJET II-04 and SIBYLL 2.3d models. Therefore, in this work, we consider the adjusted mass composition model only for SIBYLL 2.3d and QGSJET II-04, as the full implementation of EPOS-LHCR was not yet available for common air-shower simulation frameworks. Simulations using an upcoming QGSJET III model (S. Ostapchenko 2024) increase the predicted $X_{\rm max}$ scale by $\approx$5 g cm^{-2} only, leaving, however, the $X_{\rm max}$ fluctuations approximately unchanged. Finally, modifying the properties of the hadronic interactions of SIBYLL 2.3d (J. Ebr et al. 2023), the universality of $X_{\rm max}$ fluctuations for iron nuclei was confirmed to be well within $\approx$2 g cm^{-2}.

In this heavy-metal scenario, first introduced in J. Vícha et al. (2025), we discuss a novel view of the mass composition data of the Pierre Auger Observatory using two simple premises. First, we consider the possibility of shifting the $X_{\rm max}$ scale predicted by models of hadronic interactions by the same energy-independent value for all primary species while keeping all other predictions of hadronic interaction models unchanged. Second, we postulate that the data agree with expectations for pure iron nuclei above $10^{19.6}$ eV ($\approx$40 EeV). While other studies investigate the potential presence of even heavier nuclei in the cosmic-ray flux at the highest energies (see, e.g., B. D. Metzger et al. 2011; B. T. Zhang et al. 2024; G. R. Farrar 2025), triggered also by recent observation of one of the most energetic particles without the clear association of a potential source direction (R. U. Abbasi et al. 2023; M. Unger & G. R. Farrar 2024), our assumption of pure iron nuclei is based on its status as the most abundant heavy element in the Universe and the heaviest nucleus produced in significant quantities through stellar nucleosynthesis. Our two assumptions result in a generally heavier mass composition in a broad range of energies than what is obtained from the standard analyses of the $X_{\rm max}$ moments (T. Fitoussi 2023) and from the analyses that combine mass composition and spectrum information (A. Aab et al. 2017a) while resolving some tension of the muon puzzle.

The Letter is structured as follows. Section 2 describes the derivation of the shift in the predicted $X_{\rm max}$ scale from the most precise available data on $\langle X_{\rm max}\rangle$. We then present the new mass composition scenario of ultra-high-energy cosmic rays in Section 3, using four primary species by fitting the measured $X_{\rm max}$ distributions to the shifted model predictions on $X_{\rm max}$. The estimation of the consequences of this new scenario on the energy spectra of individual cosmic-ray species is given in Section 4, studies of hadronic interactions are in Section 5, and the effect on backtracking of arrival directions in the Galactic magnetic field (GMF) is presented in Section 6. We finally discuss the consistency with other studies and the possible presence of iron nuclei in cosmic-ray sources in Section 7.

2. Adjustment of the Predicted $X_{\rm max}$ Scale

The mean and standard deviation of the $X_{\rm max}$ distribution, as estimated from direct Fluorescence Detector measurements (A. Yushkov 2019), as well as from the Surface Detector data, are depicted in the left panel of Figure 1. These are presented alongside both the shifted and standard reference values of the QGSJET II-04 and SIBYLL 2.3d models. The Surface Detector data are interpreted using two methods: a deep neural network (DNN) method (A. Abdul Halim et al. 2025a) and the Δ method, which relies on a detector time-response parameter empirically proven to be correlated with $X_{\rm max}$ (C. J. Todero Peixoto 2019). It is important to note that both Surface Detector estimates are calibrated to match the Fluorescence Detector data, applying a positive shift of about 30 g cm^{-2} in the predicted $X_{\rm max}$, independently of this work.

The fluctuations of $X_{\rm max}$ above $10^{19.6}$ eV are consistent with expectations for pure iron nuclei, as predicted by the two models, with $p(\chi^2) > 0.5$. Moreover, in the same energy range, the mean $X_{\rm max}$ follows the constant elongation rate predicted for a single type of primary particle, indicating the possibility of consistently describing both $X_{\rm max}$ moments by a pure beam of particles. The χ^2 tests, given in Appendix A, also include a scenario using silicon as the only primary particle type. In such a pure-silicon scenario, the measured $X_{\rm max}$ fluctuations are well described only above $10^{19.8}$ eV, where the event statistics are very low.

The shift $\Delta X_{\rm max}$ for the $\langle X_{\rm max}\rangle$ values is obtained by assuming pure iron nuclei above $10^{19.6}$ eV and maintaining the elongation rate ($dX_{\rm max}/d\lg E$) predicted by the hadronic interaction models. In this way, we fit the $\langle X_{\rm max}\rangle$ from the Auger DNN data, obtaining $\Delta X_{\rm max} = 52 \pm 1^{+11}_{-8}$ g cm^{-2} and $\Delta X_{\rm max} = 29 \pm 1^{+12}_{-7}$ gcm^{-2} for QGSJET II-04 and SIBYLL 2.3d, respectively. These values are consistent with the results from A. Abdul Halim et al. (2024a) at the statistical level, which is not valid in the case of the pure-silicon scenario (see Appendix A).

The energy evolution of the mean and variance of $\ln A$ of the cosmic rays, interpreted (see P. Abreu et al. 2013) from the $X_{\rm max}$ distributions, is depicted in the right panel of Figure 1 alongside the interpretations using the unmodified model predictions. Note that no systematic uncertainty band is shown for $\langle \ln A\rangle$ in the case of $\Delta X_{\rm max}$, since $\langle \ln A\rangle$ is always fitted to the expectation for iron nuclei above $10^{19.6}$ eV, independently of the absolute values of the measured $X_{\rm max}$. Applying the shift $\Delta X_{\rm max}$, the energy evolution of $\langle \ln A\rangle$ and $\sigma^2(\ln A)$ consistently describes an increase in the average mass of cosmic rays as well as a decrease in the width of the mix of primary masses; as required, we arrive at a pure beam of iron nuclei at the highest energies.

Besides the overall mass shift, the $\ln A$ moments, as derived from the shifted $X_{\rm max}$ scales of the four primary particles, yield a far-reaching difference: the updated moments can be interpreted consistently within model-independent expectations. The $\ln A$ moments (before and after applying the shift in $X_{\rm max}$) are depicted in Figure 2, alongside the allowed region for all possibilities when mixing four different primary species (protons and helium, nitrogen, and iron nuclei). The moments of $\ln A$ as interpreted according to SIBYLL 2.3d and QGSJET II-04 both lie (largely) outside this *umbrella* shape. The two $\ln A$ moments obtained after the $\Delta X_{\rm max}$ shift are within the allowed region. Furthermore, the updated moments are now consistent with the results from the model-independent correlation of the depth of the shower maximum with the size of the shower footprint between 3 EeV and 10 EeV (A. Aab et al. 2016b), as

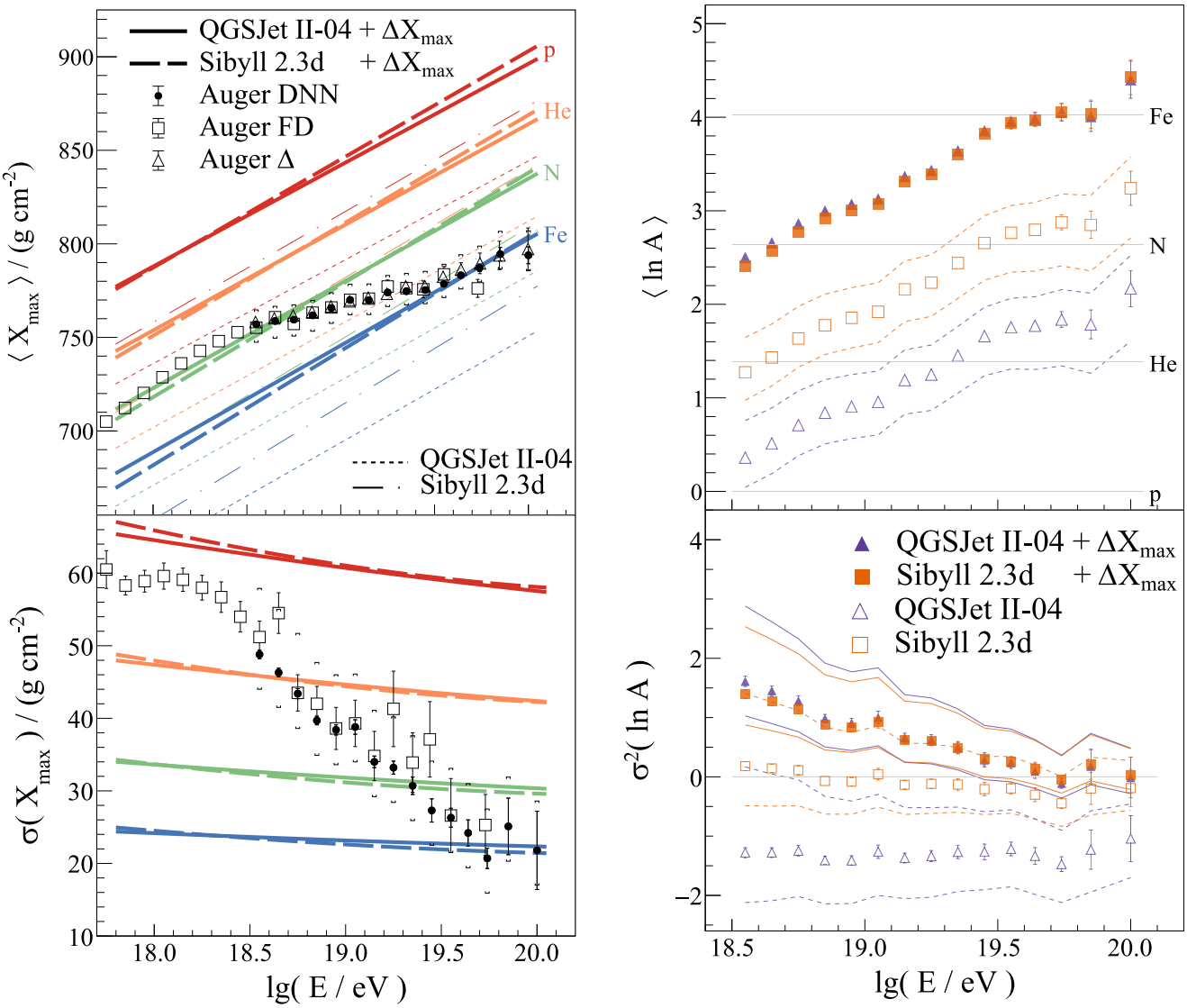

Figure 1. Left panel: the energy evolution of the mean and standard deviation of $X_{\max}$ for data (C. J. Todero Peixoto 2019; A. Yushkov 2019; A. Abdul Halim et al. 2025a) measured by the Pierre Auger Observatory (black), including the systematic uncertainty in the case of Auger DNN (brackets). The original model predictions for four primary species are depicted by thin lines and the adjusted predictions by thick lines. Right panel: the energy evolution of the two lowest moments of $\ln A$, interpreted from the Auger DNN data shown in the left panel, using the adjusted (filled markers) and original (open markers) model predictions.

indicated in Figure 2 by the dark shaded box for the corresponding energy range of $\Delta X_{\max}$ points.

3. Energy Evolution of Relative Primary Masses

To estimate the energy evolution of the relative abundance of different primary-mass species in the heavy-metal scenario, we use the $X_{\max}$ distributions published by A. Aab et al. (2014a) to fit four primary fractions (protons as well as He, N, and Fe nuclei) to the expectations from the QGSJET II-04 and SIBYLL 2.3d models after accounting for $\Delta X_{\max}$. The $X_{\max}$ distribution templates used in the fit were generated using the CONEX air-shower simulation code (T. Bergmann et al. 2007), with the same energy distribution per bin as in A. Aab et al. (2014b), and were modified to account for the effects of detector acceptance and resolution accordingly. To increase the event statistics, we merged adjacent energy bins above $10^{18.4}$ eV, reducing statistical fluctuations in the fitted primary fractions. The last energy bin is integral and includes all events with energies above $10^{19.5}$ eV. The fitted primary fractions are shown in the top panels of Figure 3, and the fitted $X_{\max}$ distributions are provided in Appendix C, along with the corresponding p-values. Overall, with SIBYLL 2.3d, we achieve sufficiently good fit qualities (p-values $\geqslant 0.05$) across the entire energy range from $10^{17.8}$ to 10^{20} eV. The QGSJET II-04 model provides an acceptable fit above $10^{18.3}$ eV but performs poorly below this energy, with p-values less than 10^{-4}.

Both hadronic interaction models favor a mass composition dominated by iron nuclei across all energies, with the iron fraction reaching a minimum between 30% and 50% at 3–4 EeV, followed by a rise to nearly 100% at the highest energies, as assumed. The energy evolution of the estimated mass composition is consistent with the transition from lighter to heavier components observed in A. Aab et al. (2014b) but with a smaller presence of lighter nuclei in the mix. The contributions of helium nuclei and protons individually remain below ≈30% at the lowest energies and decrease to below ≈10% above the ankle feature of the cosmic-ray energy

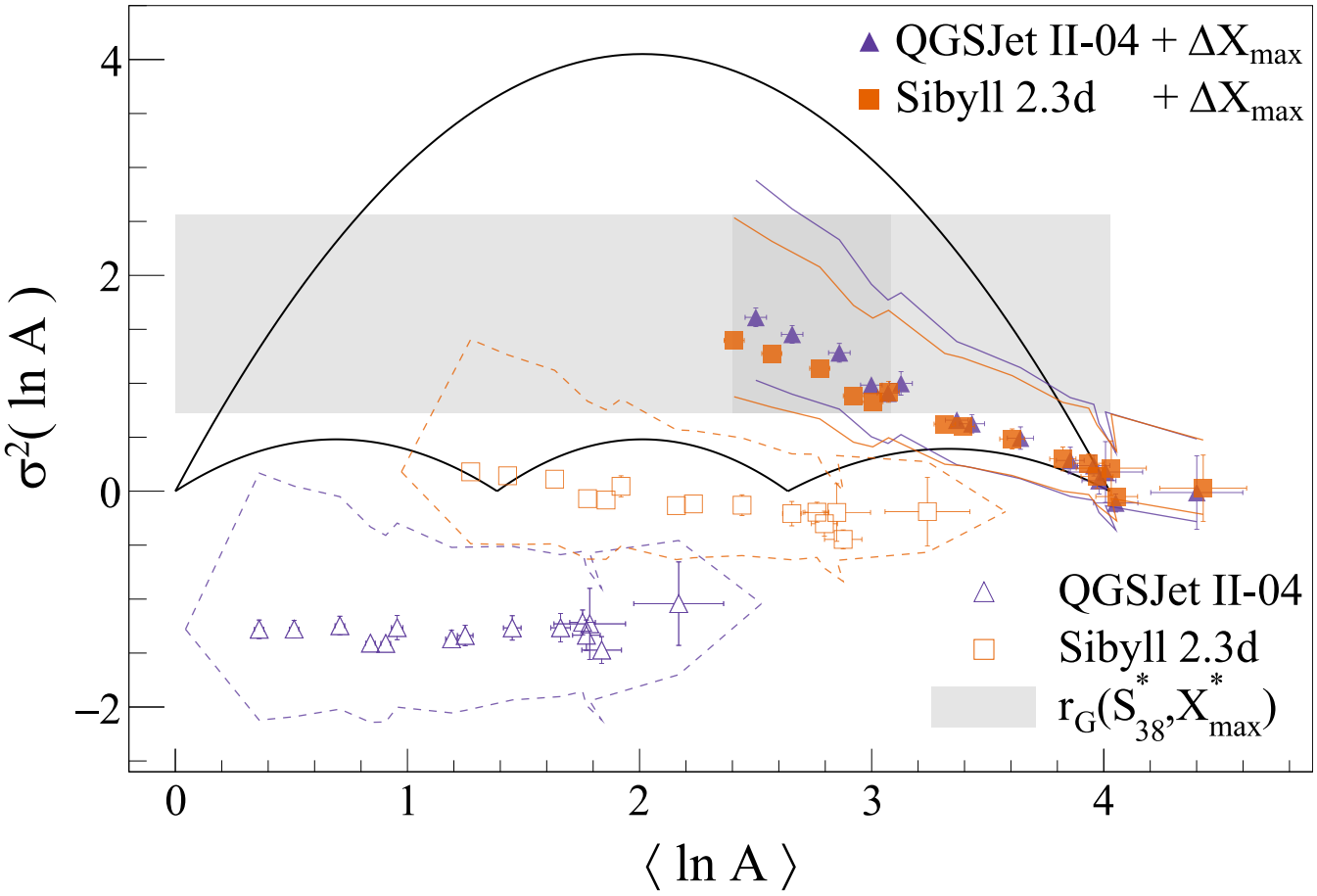

Figure 2. The relation between the interpreted moments of $\ln A$ with (filled markers) and without (open markers) the application of $\Delta X_{\max}$ to the model predictions using Auger DNN data (A. Abdul Halim et al. 2025a). The dashed and solid lines correspond to the systematic uncertainties. The range of possible combinations for p, He, N, and Fe nuclei is limited by the black lines forming the umbrella. The resulting value of $\sigma^2(\ln A)$ inferred from the correlation coefficient r_G between the ground signal and $X_{\max}$ (A. Aab et al. 2016b) for 3–10 EeV is shown by the gray band, with the darker and narrower band indicating the respective energy range of the points for $\Delta X_{\max}$.

spectrum (≈5 EeV). Above this point, around ≈10 EeV, the nitrogen fraction rises to about 30%–50% before also dropping to nearly zero at the end of the cosmic-ray spectrum.

We used two functional forms to describe the energy evolution of fitted primary fractions: a smoothed Gaussian multiplied by an exponential function and power-law functions with a simple exponential cutoff, the latter being mentioned in A. Aab et al. (2017a). The functional forms and parameters for both parameterizations are given in Appendix B. In this work, we exclusively use public data of the Pierre Auger Observatory. However, we note that including additional data will enable a more precise estimation of the primary fractions, even within the heavy-metal scenario, leading to a more accurate determination of how individual primary fractions evolve with energy.

4. Energy Spectrum of Individual Primaries

Using the primary fractions found in Section 3, we decompose the energy spectrum of cosmic rays at the highest energies into contributions from different primary nuclei. The all-particle energy spectrum[4] of cosmic rays, as measured by the Pierre Auger Observatory (A. Aab et al. 2020b), is shown in the middle panels of Figure 3. The individual contributions of the four primary species, according to the two parameterizations of primary fractions shown in the top panels, are depicted alongside the total spectrum in the respective colors. From this decomposed energy spectrum, the rigidity (E/Z) of each mass component can be inferred. The rigidity dependence of cosmic-ray flux is shown in the bottom panels of Figure 3 for the four primary species.

By assumption, the flux suppression above ≈40 EeV is caused solely by the spectral feature of iron nuclei, which might be related to the propagation effects or the maximum rigidity available at a source. Interestingly, the instep feature at ≈15 EeV in the cosmic-ray energy spectrum (A. Aab et al. 2020c) corresponds to the fading of nitrogen nuclei from the cosmic rays above this energy. The rigidity cutoffs of iron and nitrogen nuclei seem to coincide at approximately $10^{18.2}$ V, suggesting a common origin for these elements in the heavy-metal scenario. The ankle feature, meanwhile, might be connected to the fading of the light component (i.e., protons and helium nuclei) from the cosmic-ray population. However, the main limitation for these interpretations remains the statistical uncertainty in the energy evolution of primary fractions, which is especially large for protons and helium nuclei. On the other hand, their rigidity distributions might indicate, for example, the presence of a separate

[4] Note that for better visibility, the flux is scaled by the energy to the power of 3.

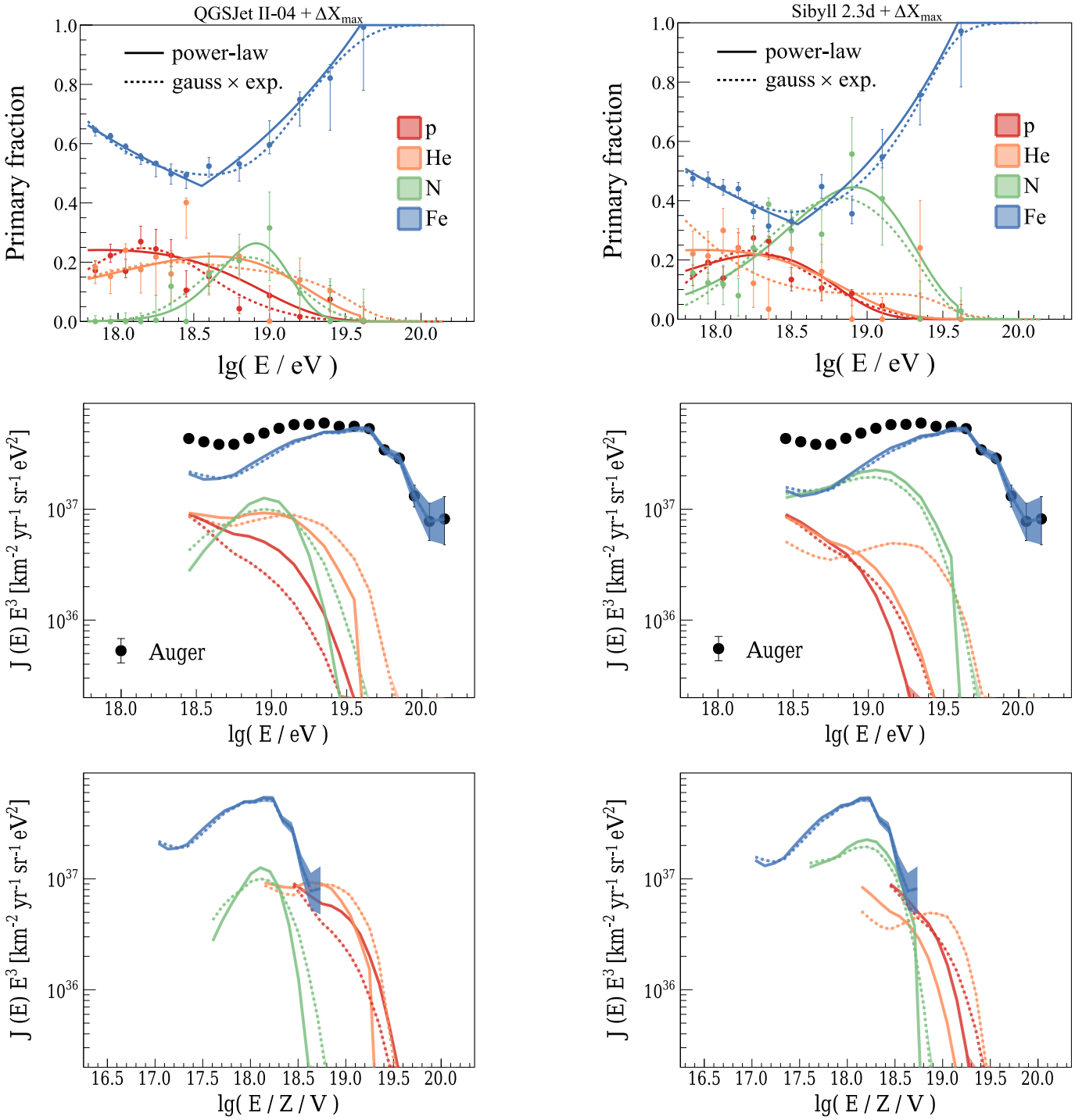

Figure 3. Energy evolution of the primary fractions (top panels) and evolution of differential fluxes of individual primary species as functions of energy (middle panels) and rigidity (bottom panels) using QGSJET II-04 + $\Delta X_{\rm max}$ (left panels) and SIBYLL 2.3d + $\Delta X_{\rm max}$ (right panels). The primary fractions were obtained by fitting the Auger $X_{\rm max}$ distributions (A. Aab et al. 2014a), while the total differential flux of cosmic rays was taken from A. Aab et al. (2020b). The two types of parameterized energy evolution of the primary fractions, see Section 3, are represented using dashed and solid lines in the panels.

population of sources with different metallicities. The constraints could be mitigated in the future by using a larger statistical sample of measured data to refine the fit of the primary fractions.

5. Hadronic Interactions

The number of muons produced in extensive air showers from ultra-high-energy cosmic rays is an interesting proxy for the amount of hadronic multiparticle production occurring in the first interactions. The mass composition is a crucial aspect when studying hadronic interactions, as it shifts the expectations in the number of muons (hadrons) produced in showers and may alleviate as well as aggravate the muon puzzle. In the following, we briefly discuss the implications of the heavy-metal scenario on the scale of the predicted number of muons and the combined effect of modified elasticity and cross section on the tail of the $X_{\rm max}$ distribution.

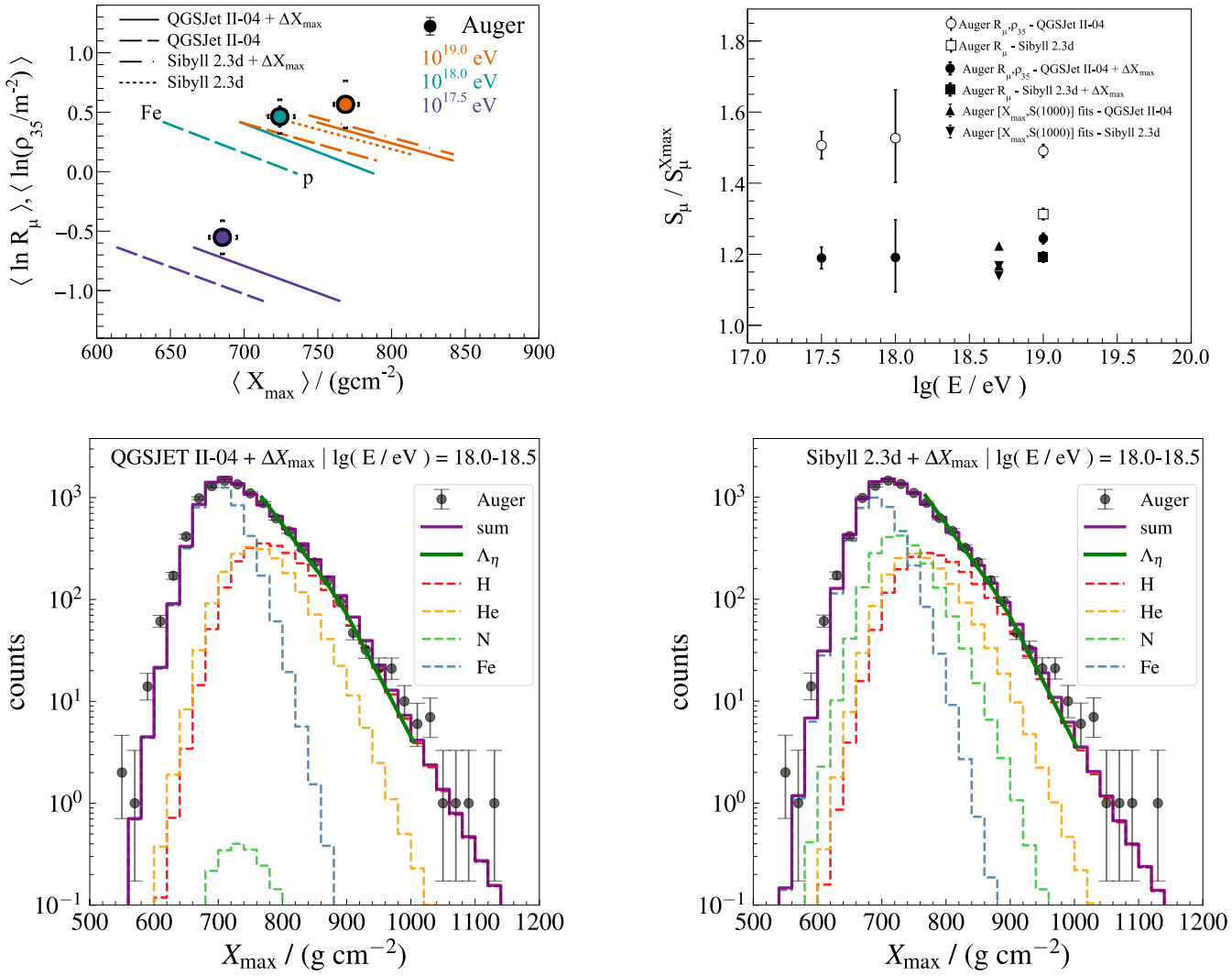

Figure 4. Top left panel: the muon number obtained by direct measurements at Auger (A. Aab et al. 2020a, 2021) compared to the predictions with and without the application of $\Delta X_{\rm max}$. Note that in case of the SIBYLL 2.3d model, only the predictions at energy 10^{19} eV were at our disposal. Top right panel: the ratio of the muon signal in the data and the signal predicted from air-shower simulations with (filled markers) and without (open markers) application of $\Delta X_{\rm max}$. The results from A. Abdul Halim et al. (2024a) are displayed by triangles. Bottom panels: the $X_{\rm max}$ distribution of Auger data (A. Aab et al. 2014a) compared to the prediction for the heavy-metal scenario (Gauss × exp.) using QGSJET II-04 + $\Delta X_{\rm max}$ (left) and SIBYLL 2.3d + $\Delta X_{\rm max}$ (right) in the energy bin $10^{18.0-18.5}$ eV. For visualization purposes, the fits to the tail of the predicted $X_{\rm max}$ distributions (Λ_η), corrected for detector acceptance, are shown.

5.1. The Number of Muons

In the top left panel of Figure 4, we present the direct measurements of the muon signal S_μ (R_μ, A. Aab et al. 2015b; ρ_{35}, A. Aab et al. 2020a) by the Pierre Auger Observatory, along with the corresponding expectations from the QGSJET II-04 and SIBYLL 2.3d models with and without applying $\Delta X_{\rm max}$, respectively. In the heavy-metal scenario, consistency with the measured $\langle X_{\rm max}\rangle$ is achieved within the systematic uncertainty for the SIBYLL 2.3d model and is nearly within the systematic uncertainty in the case of the QGSJET II-04 model.

The muon deficit in the simulated data can be assessed from the ratio of S_μ to the expectation value from simulated showers with the same average depth of the shower maximum, $\langle X_{\rm max}\rangle$ ($S_\mu^{X_{\rm max}}$). Our results are depicted in the top right panel of Figure 4. We find that the muon deficit in the expectations from the QGSJET II-04 model is reduced from about 50% to about 20%–25%. In the case of the SIBYLL 2.3d model, the lack of muons is reduced from about 30% to approximately 20%. Furthermore, the apparent muon deficit is independent of the energy of the primary particle and consistent with the findings from A. Abdul Halim et al. (2024a) using the two-dimensional fits of the ground signal at 1000 m, $S(1000)$, and $X_{\rm max}$.

5.2. Tail of the X_{max} Distribution

The tail of the $X_{\rm max}$ distribution provides essential insight into proton–air interactions, e.g., the inelastic proton–air cross section (P. Abreu et al. 2012), as proton-induced showers penetrate deeper into the atmosphere before reaching their maximum development compared to air showers initiated by heavier nuclei. We investigate how well the measured tails of $X_{\rm max}$ distributions are described within the heavy-metal scenario. A fair description of the tail of the measured $X_{\rm max}$ distribution is shown in the bottom panels of Figure 4 by the shifted model predictions in the energy bin $10^{18.0-18.5}$ eV for the QGSJET II-04 and SIBYLL 2.3d models.

We fit the $X_{\max}$ exponential shape (Λ_η) for the same $X_{\max}$ and energy range as in P. Abreu et al. (2012) for the four primaries according to our mass composition model (Gauss × exp.) applied to CONEX air-shower simulations smeared by the $X_{\max}$ resolution according to A. Aab et al. (2014a). The resulting values, $\Lambda_\eta = (51.9 \pm 0.4)\,\mathrm{g\,cm^{-2}}$ and $\Lambda_\eta = (50.0 \pm 0.4)\,\mathrm{g\,cm^{-2}}$ for QGSJET II-04 + $\Delta X_{\max}$ and SIBYLL 2.3d + $\Delta X_{\max}$, respectively, are smaller than the value $\Lambda_\eta = (55.8 \pm 2.3(\mathrm{stat}) \pm 1.6(\mathrm{sys}))\ \mathrm{gcm^{-2}}$ obtained from the Auger data (P. Abreu et al. 2012). The smaller predicted values of Λ_η in the heavy-metal scenario might be explained by a larger helium fraction, larger p–p inelastic cross section, or lower elasticity extrapolated in the two models from accelerator measurements, which is qualitatively in line with the extrapolations used in the updated EPOS-LHC model (T. Pierog & K. Werner 2023) and predicted by studies of modifications of hadronic interactions (J. Ebr et al. 2023). In the case of unmodified QGSJET II-04 and SIBYLL 2.3d $X_{\max}$ distributions, we obtain $\Lambda_\eta = (55.2 \pm 0.4)\,\mathrm{g\,cm^{-2}}$ and $\Lambda_\eta = (52.1 \pm 0.4)\,\mathrm{g\,cm^{-2}}$, respectively, as a consequence of a lower helium fraction with respect to the heavy-metal scenario. We emphasize that, in any case, our Λ_η values are not directly comparable to those published by the Pierre Auger Collaboration, as all detector and event-selection effects have not been taken into account in our calculation. However, this approach represents the best possible comparison within our limitations. Note that a more sophisticated method to derive the inelastic p–p cross section is needed to accurately account for a mixed mass composition (O. Tkachenko et al. 2021).

6. Arrival Directions

Cosmic rays are subject to magnetic deflections during their propagation from the source to the Earth. The dipole anisotropy observed in the arrival directions of cosmic rays above 8 EeV suggests their extragalactic origin (A. Aab et al. 2017b; A. Abdul Halim et al. 2024b).

In this section, we demonstrate the effect of the GMF on the arrival directions by backtracking the cosmic rays as their antiparticles, assuming their mass according to the heavy-metal scenario. First, we study the possible features of an extragalactic dipole in the distribution of cosmic-ray arrival directions, consistent with the observed dipole above 8 EeV, after accounting for the effects of the GMF. Second, we derive the region in the sky from which the most energetic events (A. Abdul Halim et al. 2023a), above 78 EeV, might come, assuming they all are iron nuclei.

6.1. Features of an Extragalactic Dipole

Assuming an ideal dipole distribution of the cosmic-ray flux at the edge of the Galaxy (20 kpc from the Galactic center), we constrain the range of possible extragalactic features of the dipole by repeating the analysis from A. Bakalová et al. (2023), using new models of the GMF and the mass composition scenario for SIBYLL 2.3d + $\Delta X_{\max}$ proposed in this work (see the dotted lines in the top right panel of Figure 3 and Appendix B.1). The propagation of cosmic rays in the GMF is simulated with CRPropa 3 (R. Alves Batista et al. 2022). We use the eight models of the coherent component of the GMF from M. Unger & G. R. Farrar (2024; UF23) with the turbulent component from the model of the GMF by R. Jansson & G. R. Farrar (2012; JF12) and apply the corrections from the Planck Collaboration (R. Adam et al. 2016). The simulations were performed for three values of the coherence length of the turbulent component, $l_c = 30$ pc, 60 pc, and 100 pc, with multiple realizations of the turbulent field for each l_c. The extragalactic direction of the dipole is imposed in all possible longitudes and latitudes with a step of 1°, and the extragalactic amplitude of the dipole A_0 is explored in the range from 6% up to 30% in discrete steps of 2% and from 30% up to 100% in discrete steps of 10%. We compare the reconstructed amplitude and the direction of the dipole on Earth from the simulations with the measured values by the Pierre Auger Observatory, an amplitude of $7.4^{+1.0}_{-0.8}$%, and a direction in equatorial coordinates $(\alpha, \delta) = (97° \pm 8°, -38° \pm 9°)$ from A. Abdul Halim et al. (2024b).

The identified possible extragalactic directions that are compatible with the direction and amplitude measurement from the Pierre Auger Observatory at the 1σ and 2σ levels are shown in the top panel of Figure 5 for the combination of all eight UF23 models of the GMF (see Appendix D for the solutions corresponding to each individual UF23 model and the effect of different coherence lengths of the turbulent component). Note that possible extragalactic directions of the dipole at the 1σ level were identified only for amplitudes above 40%. All extragalactic dipoles identified in this work have an initial amplitude of $A_0 \geqslant 12\%$ (see Appendix D). The identified areas of possible extragalactic directions are consistent with the previously published results from A. Bakalová et al. (2023), where no specific mass composition was assumed, and different GMF models were used. The direction of the 2 Micron All-Sky Redshift Survey dipole (P. Erdoğdu et al. 2006; 2MRS), which approximately describes the distribution of matter in the local Universe, is located within the identified region at the 2σ level. The large amplitudes of an extragalactic dipole identified in this work are a consequence of the heavy mass composition assumption. Achieving such high amplitudes through the source distribution alone is challenging, unless only a small number of sources contribute significantly to the flux above 8 EeV.

As suggested by other studies, a physically motivated source distribution following the large-scale structure of the Universe can also lead to a dipole anisotropy on Earth compatible with the measurements of the Pierre Auger Observatory (D. Harari et al. 2015; C. Ding et al. 2021; T. Bister et al. 2024). However, the mass composition of the cosmic-ray flux assumed in these studies is lighter than in the heavy-metal scenario.

6.2. Arrival Directions at the Highest Energies

We backtrack the 100 most energetic events (above 78 EeV) measured by the Pierre Auger Observatory from A. Abdul Halim et al. (2023a) to the edge of the Galaxy, assuming that all the particles are iron nuclei. Similarly to Section 6.1, we combine the coherent UF23 models with the turbulent field from the JF12 model, including the Planck Collaboration corrections, and use multiple realizations of the turbulent field for three different coherence lengths. For each event, we backtrack 200 anti-iron nuclei, with their arrival directions smeared by a 1° directional uncertainty, using a flat distribution around the reconstructed direction. The energy is smeared by a Gaussian distribution, accounting for the uncertainty in the reconstructed energy. This backtracking procedure is then repeated for an isotropic distribution of

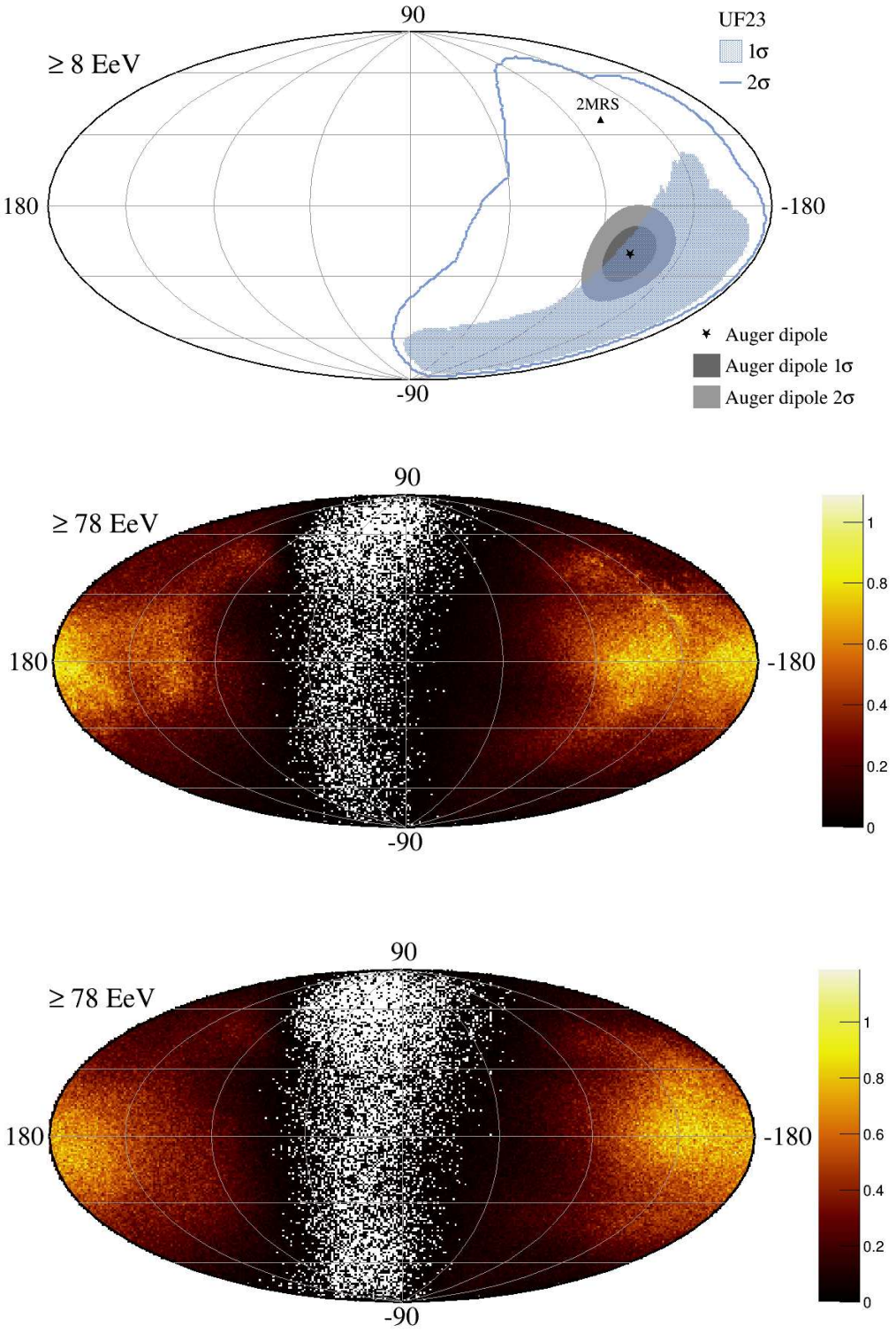

Figure 5. Top panel: possible directions of an extragalactic dipole in the arrival directions of cosmic rays above 8 EeV, compatible at the 1σ (blue area) and 2σ (blue contour) levels with the Auger measurement (A. Aab et al. 2017b), for the UF23 models of the GMF, shown in Galactic coordinates. The mass composition scenario obtained for SIBYLL 2.3d + $\Delta X_{\rm max}$ is used. Middle panel: the distribution of backtracked directions at the edge of the Galaxy for the 100 most energetic Auger events (A. Abdul Halim et al. 2023a), shown in Galactic coordinates. Bottom panel: distribution of the backtracked directions at the edge of the Galaxy for isotropically distributed arrival directions of iron nuclei on Earth, shown in Galactic coordinates and accounting for the Auger geometrical exposure.

arrival directions, using the same energies as those of the detected events and corrected for the directional exposure of the Auger surface detector (P. Sommers 2001).

The normalized histogram of the backtracked directions of the most energetic Auger events at the edge of the Galaxy is shown in the middle panel of Figure 5 in the Galactic

coordinates. This plot combines the simulations of all the different realizations of the GMF. Assuming only iron nuclei, the sources of these particles are predominantly located in the direction of the Galactic anticenter. This behavior is strongly influenced by the low rigidity of the particles in the heavy-metal scenario and the GMF, which causes the demagnification of sources in the direction of the Galactic center. A similar behavior is expected for an isotropic distribution of the arrival directions (see the bottom panel of Figure 5).

The ratio of the distributions obtained from the backtracked Auger events and the backtracked isotropically distributed arrival directions on Earth is shown in Appendix D. The excess regions seem to follow the supergalactic plane, with the largest excess in the vicinity of the Centaurus A/M83 group. However, these excesses may result from the low statistics of the observed extremely energetic events or from specific features of the UF23 model of the GMF. A more thorough investigation of these effects is beyond the scope of this Letter.

7. Discussion

7.1. Consistency with Other Studies

The interpretation of the data of the Pierre Auger Observatory becomes surprisingly consistent when assuming a simple but also extreme scenario in which the mass composition of cosmic rays at the flux suppression is dominated by iron nuclei. After applying $\Delta X_{\max}$, the resulting moments of the logarithmic nuclear mass, $\ln A$, fall within the physical range expected for protons and He, N, and Fe nuclei; see Figure 2. Furthermore, the value of $\sigma^2(\ln A)$ in the energy range $10^{18.5}$–10^{19} eV is consistent with the model-independent constraints from A. Aab et al. (2016b). For the QGSJET II-04 model, clear indications of too-shallow $X_{\max}$ predictions had already been claimed in the latter study, when the inferred primary-mass mixing was compared to that obtained from the fits of $X_{\max}$ distributions. Moreover, in A. Aab et al. (2017a), shifting the $X_{\max}$ scale of the models to some extent resulted in a more coherent picture of the mass composition data from the Pierre Auger Observatory.

Interestingly, the mass estimates obtained from the surface-detector-reconstructed $X_{\max}$ (A. Aab et al. 2017; A. Abdul Halim et al. 2025a), without calibration to the values measured by the fluorescence telescopes, are consistent with the mass composition scenario proposed in this work. However, this could just be coincidental, as the results of the two methods might be affected by the lack of muons in the simulated ground signal.

The interpretation of arrival directions measured by the Telescope Array experiment was found to be in better agreement with a heavier mass composition (R. U. Abbasi et al. 2024) than that obtained by the Pierre Auger Collaboration in A. Aab et al. (2017b), which is again consistent with our heavy-metal scenario. The modeled descriptions of the Auger dipole in arrival directions above 8 EeV, with a source distribution following the large-scale structure (A. Abdul Halim et al. 2024b), indicate that a heavier mass composition than that inferred using the standard model predictions could better explain the observed dipole amplitude, which is smaller than initially anticipated.

An indication of alleviation of the muon problem is also apparent when estimating the number of muons from the data of the Pierre Auger Observatory using a four-component shower universality model (M. Stadelmaier et al. 2024) applied to the combined fluorescence and surface detector data (M. Stadelmaier 2023). In the latter work, the number of hadronic shower particles at the ground is estimated from the independent fluorescence detector measurements of the shower development and the primary energy, thereby suppressing the sensitivity of the muon-scale estimation to the predicted $X_{\max}$ scale.

In the future, an update of the EPOS-LHC model of hadronic interactions will shift the $X_{\max}$ scale for expectations deeper for the four primary particles, implying a heavier mass composition than previously assumed (T. Pierog & K. Werner 2023), approximately at the level of the $X_{\max}$ scale suggested in this work.

7.2. Iron Nuclei in Cosmic-Ray Source Candidates

The energy flux J of cosmic rays above $10^{19.6}$ eV can be determined by integrating the cosmic-ray energy spectrum from A. Aab et al. (2020b):

$$J(>10^{19.6}\ \mathrm{eV}) = \int_{10^{19.6}\ \mathrm{eV}}^{10^{20.15}\ \mathrm{eV}} E\, J(E)\, dE. \tag{1}$$

We find that $J(>10^{19.6}\ \mathrm{eV}) \sim 4.5 \times 10^{17}\ \mathrm{eV\,km^{-2}\,yr^{-1}\,sr^{-1}}$. To calculate the luminosity density Q of these cosmic rays, we use

$$Q(>10^{19.6}\ \mathrm{eV}) \approx \frac{4\pi\, J(>10^{19.6}\ \mathrm{eV})}{D_{\mathrm{loss}}}, \tag{2}$$

where D_{loss} represents the characteristic energy loss length of the particles. Previous studies have discussed the propagation of iron nuclei with energies in the range 10^{19}–10^{20} eV, finding $D_{\mathrm{loss}} \approx 100$ Mpc (D. Allard et al. 2005; Y. Jiang et al. 2021). However, as we want the particles to arrive at the Earth retaining their iron identity, we adopt as D_{loss} the attenuation length used in our simulations above 40 EeV, which is approximately 30 Mpc. With this, we find the required luminosity density to be $Q(>10^{19.6}\ \mathrm{eV}) \approx 3 \times 10^{44}\ \mathrm{erg\,Mpc^{-3}\,yr^{-1}}$.

It is reasonable to consider that, at the source, there may also be lighter elements that are accelerated up to lower energies due to their lower atomic numbers. Indeed, our results in the bottom panels of Figure 3 suggest a common origin for the nitrogen component as well. Assuming a particle injection spectrum $Q(E) = Q_0\, E^{-\gamma}$ with $\gamma = 2$ at the sources, covering energies from 10^{18} to 10^{20} eV, the normalization constant Q_0 can be determined by requiring the distribution to match $Q(>10^{19.6}\ \mathrm{eV})$:

$$\begin{aligned} Q(>10^{19.6}\ \mathrm{eV}) &= \int_{10^{19.6}\ \mathrm{eV}}^{10^{20.15}\ \mathrm{eV}} E\, Q(E)\, dE \\ &= Q_0 \ln\left(\frac{10^{20.15}\ \mathrm{eV}}{10^{19.6}\ \mathrm{eV}}\right). \end{aligned} \tag{3}$$

Using this value, we can calculate the integrated luminosity density of the sources over the energy range 10^{18}–$10^{20.15}$ eV, yielding $Q_{\text{CR-source}} \approx 10^{45}\ \mathrm{erg\,Mpc^{-3}\,yr^{-1}}$. Considering that the typical efficiency of the cosmic-ray acceleration is 10% or less, the sources would need to have a luminosity density of at least $10^{46}\ \mathrm{erg\,Mpc^{-3}\,yr^{-1}}$. This criterion narrows down the list of potential candidate sources for ultra-high-energy cosmic rays to blazars, radio galaxies, hard X-ray active galactic nuclei (AGNs), and accretion shocks in galaxy cluster mergers, as only these sources are likely to meet the required luminosity

density (see, e.g., K. Murase & M. Fukugita 2019). Both galaxy clusters and hard X-ray AGNs show evidence of high abundance of iron nuclei. In galaxy clusters, concentrations of iron nuclei are estimated to reach higher levels in the central regions (A. Liu et al. 2020). Similarly, hard X-ray AGNs also exhibit significant iron content, with inferred values exceeding the solar abundance (S. Komossa & S. Mathur 2001 and references therein). Observations of specific radio galaxies suggest that iron concentrations peak near their centers as well, reaching values close to solar metallicity (see, e.g., N. Werner et al. 2006). Among these sources, hard X-ray AGNs are the most abundant in the nearby Universe, while blazars are the rarest. Taking into account the iron attenuation length of 30 Mpc, the most favored sources are hard X-ray AGNs and radio galaxies. If, instead of assuming a power-law particle injection with an index $\gamma = 2$, a spectral index $\gamma = 1$ is considered, then $Q_{\text{CR-source}} \approx 4 \times 10^{44}\,\text{erg}\,\text{Mpc}^{-3}\,\text{yr}^{-1}$ is obtained. This harder particle distribution would also make starburst galaxies viable candidates, though only marginally, as they would just meet the minimum energy requirement.

To estimate the level of expected purity of a beam of iron nuclei at Earth, we consider uniformly distributed sources from 3 Mpc up to 150 Mpc with the source density $\rho = 10^{-4}\,\text{Mpc}^{-3}$ producing iron nuclei with an energy spectrum following the power law with spectral index $\gamma = 2$ and an exponential rigidity cutoff for two values of R_{cut} of 3 EV and 5 EV. Using the simulated energy losses on the cosmic microwave background and the extragalactic background light (R. C. Gilmore et al. 2012), we find that $\langle \ln A \rangle$ on Earth above 40 EeV is above ∼3.8, and $\sigma^2(\ln A)$ is below ∼0.03. This shows that the propagation has a small effect on the mass composition above 40 EeV, preserving the scenario suggested in this Letter.

8. Conclusions

We have presented a data-driven mass composition scenario for ultra-high-energy cosmic rays, in which we attempt to achieve a physically consistent interpretation of the depth of the shower maximum (X_{max}) measured by the Pierre Auger Observatory. To this end, we assume an extreme astrophysical benchmark scenario in which the cosmic-ray flux above ≈40 EeV consists purely of iron nuclei and allows for shifts in the expected X_{max} scale of the two models of hadronic interactions, QGSJET II-04 and SIBYLL 2.3d. The resulting shifts of the predicted X_{max} scale to deeper values closely match those obtained from joint fits of X_{max} and the ground signal distributions at 3–10 EeV (A. Abdul Halim et al. 2024a). Such a shift of the predicted X_{max} scale might be explained by recent improvements in air-shower modeling (T. Pierog & K. Werner 2023). Consequently, the changes in the mean and variance of $\ln A$ shift the measured data at 3–100 EeV within the region of expected combinations of protons and He, N, and Fe nuclei, contrary to the standard interpretation using unmodified model predictions. The variance of $\ln A$ is then consistent with the model-independent constraints on the broadness of the cosmic-ray mass composition at energies of 3–10 EeV (A. Aab et al. 2016b). Furthermore, we discussed the implications of this scenario on the consistency of the decomposed energy spectrum, hadronic interaction studies, and backtracked arrival directions.

In the presented heavy-metal scenario, the flux suppression of cosmic rays is consistent with a rigidity cutoff at approximately 2 EV. Consequently, nitrogen and iron nuclei starting to disappear from the cosmic rays at the same rigidity could explain the instep feature of the cosmic-ray energy spectrum. The deficit of muons predicted by QGSJET II-04 and SIBYLL 2.3d, compared to direct measurements of the muon signal, is alleviated from ∼30%–50% to ∼20%–25%, approximately independently of the primary energy. There is an indication that the inelastic p–p cross section or elasticity needs to be modified in SIBYLL 2.3d or QGSJET II-04 within the heavy-metal scenario at $10^{18.0-18.5}$ eV; however, the overall description of the X_{max} distribution remains reasonable within the statistical uncertainties. Considering the observed dipole anisotropy of ultra-high-energy cosmic rays at energies above 8 EeV, we confirm that this observation is consistent with a possible extragalactic dipolar distribution of cosmic-ray sources within the heavy-metal scenario at the 2σ level and even at the 1σ level for very high extragalactic amplitudes (above ∼40%). Assuming only iron nuclei, the arrival directions of the most energetic Auger events, when backtracked through the GMF, point toward the Galactic anticenter region, which is consistent with the expectations from isotropic arrival directions at the Earth. The estimated integrated luminosity density of the sources within the heavy-metal scenario suggests that only very powerful objects, such as hard X-ray AGNs, could explain the origin of the ultra-high-energy cosmic rays.

Acknowledgments

The work was supported by the Czech Academy of Sciences, LQ100102401; Czech Science Foundation, 21-02226M; Ministry of Education, Youth and Sports, Czech Republic, FORTE CZ.02.01.01/00/22_008/0004632; and German Academic Exchange service (DAAD PRIME). The authors are very grateful to the Pierre Auger Collaboration for discussions about this work, especially to G. R. Farrar and M. Unger.

Appendix A
Purity of the Primary Beam

We apply the χ^2 test to check the consistency of a pure beam of Fe and Si nuclei above a given energy, as shown in Figure 6. For this, we use the elongation rate and X_{max} fluctuations predicted by the QGSJET II-04 and SIBYLL 2.3d models, comparing them with the Auger DNN data (A. Abdul Halim et al. 2025a). In the case of the elongation rate test, the energy evolution was fitted with the model prediction, allowing freedom in the X_{max} scale. These tests show compatibility with a pure beam of Fe nuclei above $10^{19.6}$ eV in both X_{max} moments. In the case of the Si nuclei, a consistent description of both X_{max} moments can only be achieved at higher energies than for Fe nuclei, where the event statistics become very low. This inconsistency is caused by the poor description of X_{max} fluctuations, which would be even worse for lighter nuclei than Si. Note also that in the case of pure Si nuclei at the highest energies, the obtained X_{max} shifts are $(36 \pm 1)\,\text{g}\,\text{cm}^{-2}$ and $(12 \pm 1)\,\text{g}\,\text{cm}^{-2}$ for QGSJET II-04 and SIBYLL 2.3d, respectively, which is in tension with the results from A. Abdul Halim et al. (2024a), even when accounting for

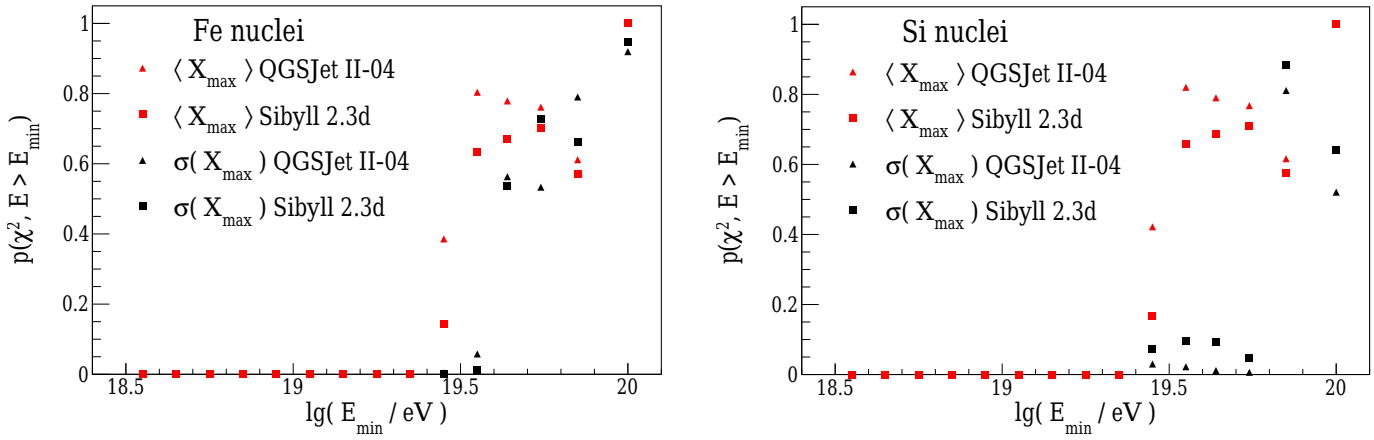

Figure 6. Test of beam purity for iron nuclei (left) and silicon nuclei (right) above the energy $E_{\rm min}$ using the Auger DNN data (A. Abdul Halim et al. 2025a). The p-values of the χ^2 test for a constant elongation rate of a single primary type above $E_{\rm min}$ (in red) and for $X_{\rm max}$ fluctuations consistent with pure nuclei above $E_{\rm min}$ (in black).

the systematic uncertainties, which are highly correlated between these two results.

Appendix B
Functional Forms of the Energy Evolution of the Primary Fractions

We use two different functional forms to describe the energy evolution of the fitted primary fractions shown in the top panels of Figure 3. The Gauss × exponential function provides a purely empirical description of the energy evolution of the primary fractions, while the power-law function with a simple exponential cutoff allows for a more physically motivated description of the energy evolution of the primary fractions, as discussed in A. Aab et al. (2017b).

B.1. Gauss × Exponential Function

The smoothed description of the energy evolution of the primary fractions $i = $ p, He, N, and Fe is obtained by a log-likelihood minimization using the following functions:

$$\hat{f}_i = A_i \exp\left[-\frac{(\lg(E/\mathrm{eV}) - \mu_i)^2}{2\sigma_i^2}\right] \times f_{\rm exp}\,, \tag{B1}$$

where

$$f_{\rm exp} = \frac{1}{1 + \exp\left[10\,(\lg(E/\mathrm{eV}) - W_i)\right]}, \tag{B2}$$

if $i = $ p, He, or N. For Fe nuclei, we set $f_{\rm exp} = 1$. The final primary functions, which are minimized simultaneously, are normalized to $\sum f_i = 1$ using

$$f_i = \hat{f}_i / \sum \hat{f}_i\,. \tag{B3}$$

The resulting fitted parameters are given in Table 1.

B.2. Power-law Function with a Simple Exponential Cutoff

We also considered a description of the energy evolution of the primary fractions using a power-law function with a simple exponential cutoff above the decimal logarithm (lg) of energy

Table 1
Parameters of the Energy Evolution of Primary Fractions for Gauss × Exponential Function

	A_i	μ_i	σ_i	W_i	A_i	μ_i	σ_i	W_i
$i = $ p	1.248	18.237	0.405	19.659	0.001	18.454	0.372	19.509
$i = $ He	1.077	18.486	0.624	19.659	0.004	1254.368	640.098	19.509
$i = $ N	1.128	18.805	0.288	19.659	0.003	18.874	0.405	19.509
$i = $ Fe	2.739	20.089	11.368	⋯	25.661	35.606	3.95	⋯

Note. Parameters of the Gauss × exponential function fitted to the energy evolution of the primary fractions in the top panels of Figure 3 for QGSJET II-04 (left) and SIBYLL 2.3d (right).

Table 2
Parameters of the Energy Evolution of Primary Fractions for Power-law Function

	a_i	b_i	c_i	Y_i	a_i	b_i	c_i	Y_i
$i = $ p	0.104	−2.87	⋯	18.87	0.644	−12.60	⋯	18.48
$i = $ He	0.402	−8.41	⋯	19.03	0.144	−3.58	⋯	18.75
$i = $ N	3.479	−65.30	⋯	18.37	1.022	−19.67	⋯	18.91
$i = $ Fe	−0.214	⋯	0.325	18.55	−0.270	⋯	0.467	18.54

Note. Parameters of the power-law functions fitted to the energy evolution of the primary fractions in the top panels of Figure 3 for QGSJET II-04 (left) and SIBYLL 2.3d (right).

Y_i, except for Fe nuclei. For $i = $ p, He, and N nuclei, we use for the χ^2 minimization of the primary fractions

$$\lg f_i = a_i \lg(E/\mathrm{eV}) + b_i + \lg(e)\,(1 - 10^{\lg(E/\mathrm{eV}) - Y_i}). \quad \text{(B4)}$$

In the case of the Fe nuclei, we use power-law functions with a break at lg energy Y_{Fe} and force the fraction of iron nuclei to be 1 above the energy $10^{19.6}$ eV:

$$\lg f_{\mathrm{Fe}} = a_{\mathrm{Fe}}\,(\lg(E/\mathrm{eV})) - Y_{\mathrm{Fe}}) + c_{\mathrm{Fe}}\,(Y_{\mathrm{Fe}} - 19.6), \quad \text{if } \lg(E/\mathrm{eV}) < Y_{\mathrm{Fe}}, \quad \text{(B5)}$$

$$\lg f_{\mathrm{Fe}} = a_{\mathrm{Fe}}\,(\lg(E/\mathrm{eV}) - Y_{\mathrm{Fe}}), \quad \text{if } Y_{\mathrm{Fe}} \leqslant \lg(E/\mathrm{eV}) \leqslant 19.6, \quad \text{(B6)}$$

$$\lg f_{\mathrm{Fe}} = 0, \quad \text{if } 19.6 \leqslant \lg(E/\mathrm{eV}). \quad \text{(B7)}$$

The resulting fitted parameters are given in Table 2. Note that these parameterizations do not satisfy $\sum f_i = 1$ within ≈15%.

Appendix C
X_{max} Distributions of the Fraction Fit

We plot the Auger X_{max} distributions (A. Aab et al. 2014a) together with the simulated predictions and individual contributions of the four primaries in Figure 7 for Sibyll 2.3d + ΔX_{max} and in Figure 8 for QGSJet II-04 + ΔX_{max}. For each hadronic interaction model, the energy binning intervals above $10^{18.4}$ eV were defined by merging adjacent bins based on the observed fluctuations in the fractions fitted with a step size of $\lg(E/\mathrm{eV}) = 0.1$.

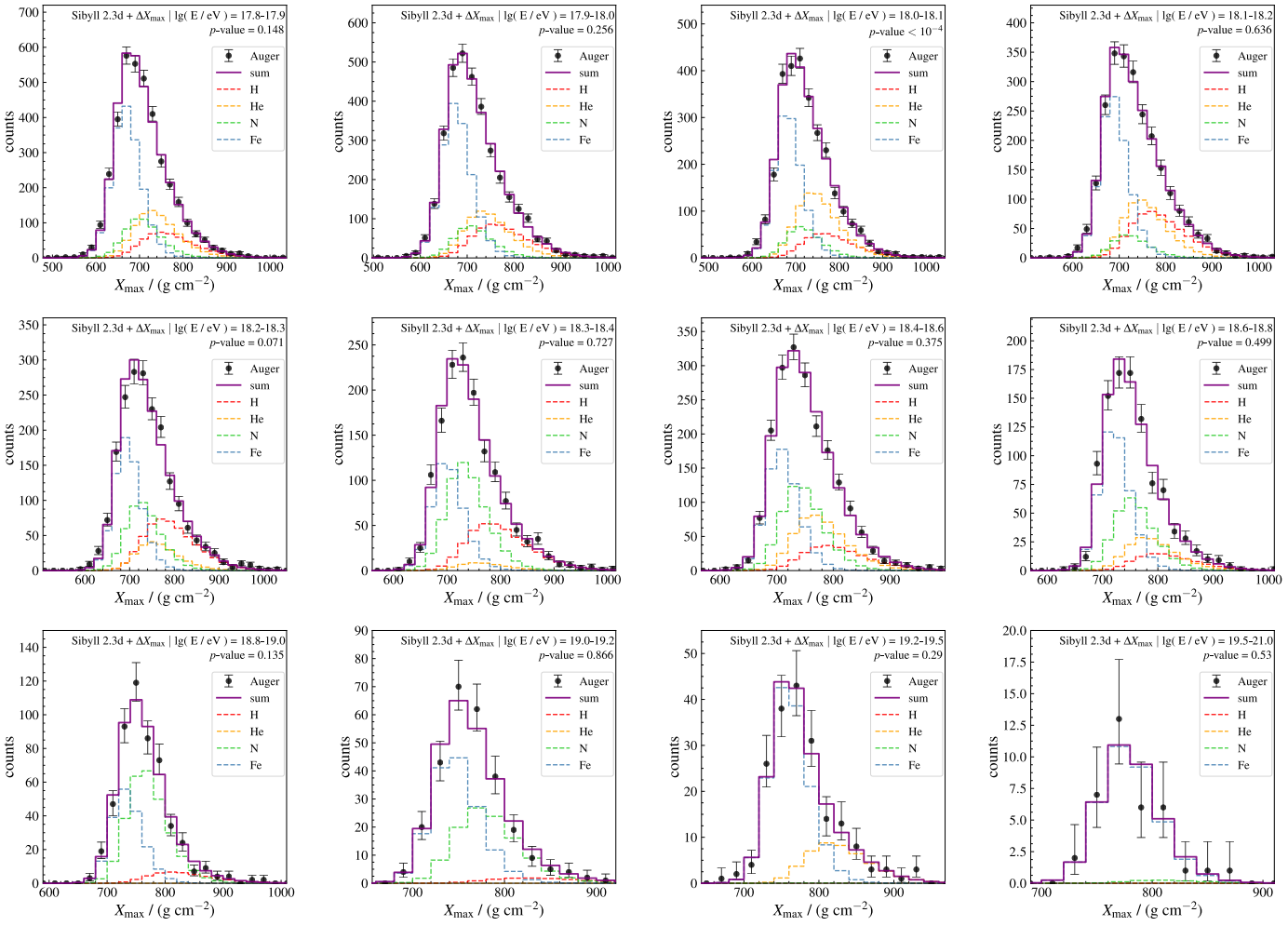

Figure 7. Distributions of X_{max} obtained from fits in each energy bin using the model Sibyll 2.3d + ΔX_{max}. The plot shows the total fit (sum) alongside the individual contributions of particle species. The p-value of the fit and the energy bin for which the fit is performed are indicated in each panel.

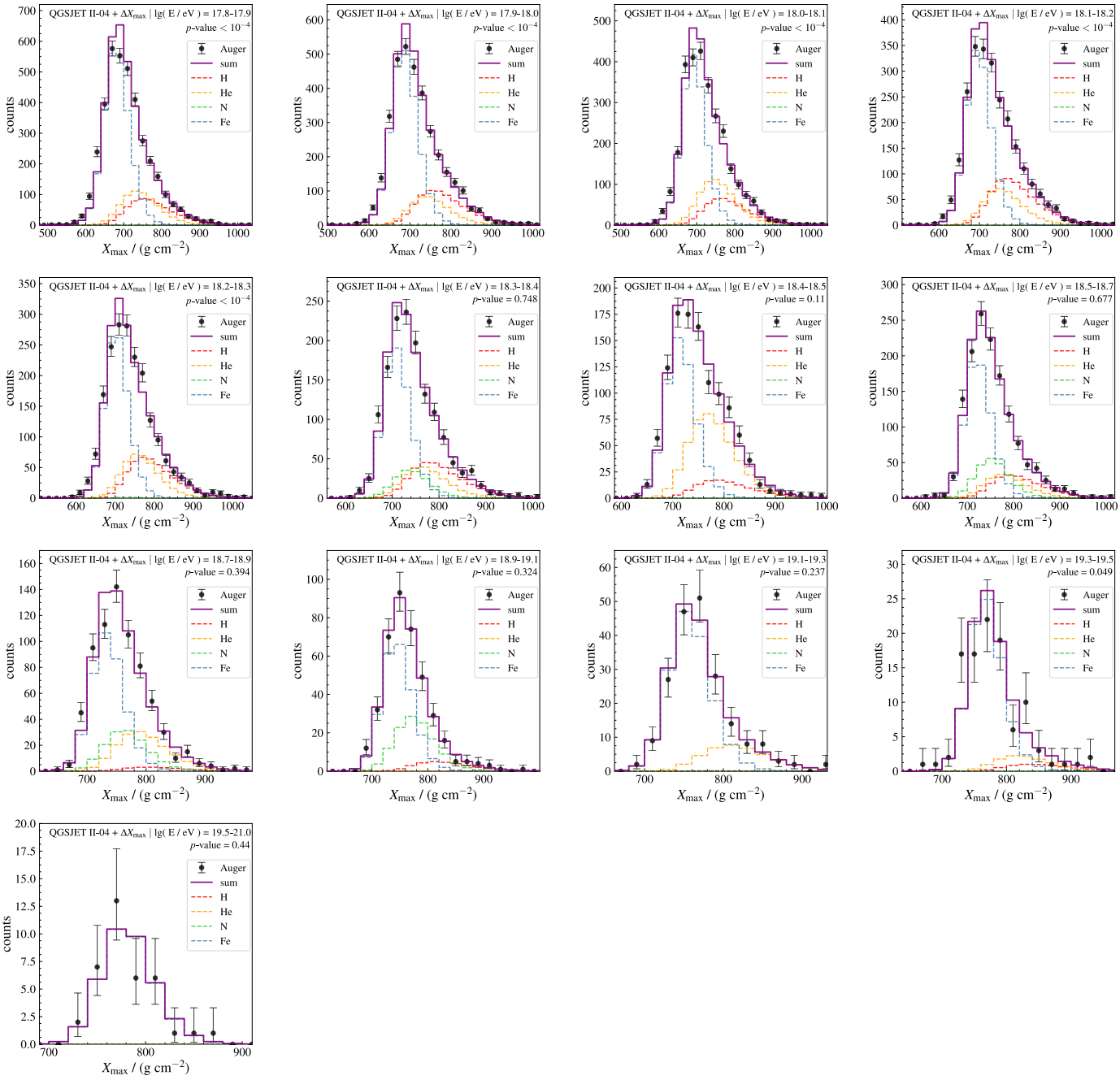

Figure 8. Same as Figure 7 but for model QGSJET II-04 + $\Delta X_{\rm max}$.

Appendix D
Arrival Directions

The 1σ and 2σ regions of the identified possible extragalactic directions of the dipole for individual UF23 models of the GMF are depicted in the middle panel of Figure 9, while the bottom panel shows the identified possible extragalactic directions of the dipole for three different coherence lengths of the turbulent field for the case of the UF23 base model.

The normalized distribution of the extragalactic amplitudes of the identified possible solutions of the dipole from Section 6.1 is shown in the top panel of Figure 9 for the individual UF23 models of the GMF. As the mass composition of the cosmic rays in the scenario proposed in this work is dominated by heavy nuclei, the required extragalactic amplitude of the dipole is rather large ($A_0 \geqslant 12\%$) in order to obtain a dipole amplitude on Earth compatible with the measured one. We decided to include extragalactic amplitudes as high as 100% for completeness. However, such high amplitudes cannot be easily explained by the spatial distribution of many sources and could only be achieved if a small number of sources contribute to the cosmic-ray flux above 8 EeV. We note that the maximum trajectory length of the simulated particles is set to 500 kpc. However, even for iron nuclei, the vast majority of the simulated particles have much shorter trajectory lengths, typically in the range $\sim$(20–100) kpc.

In Figure 10, we show the distribution of the backtracked directions at the edge of the Galaxy for the isotropically distributed arrival directions on Earth with the same energies

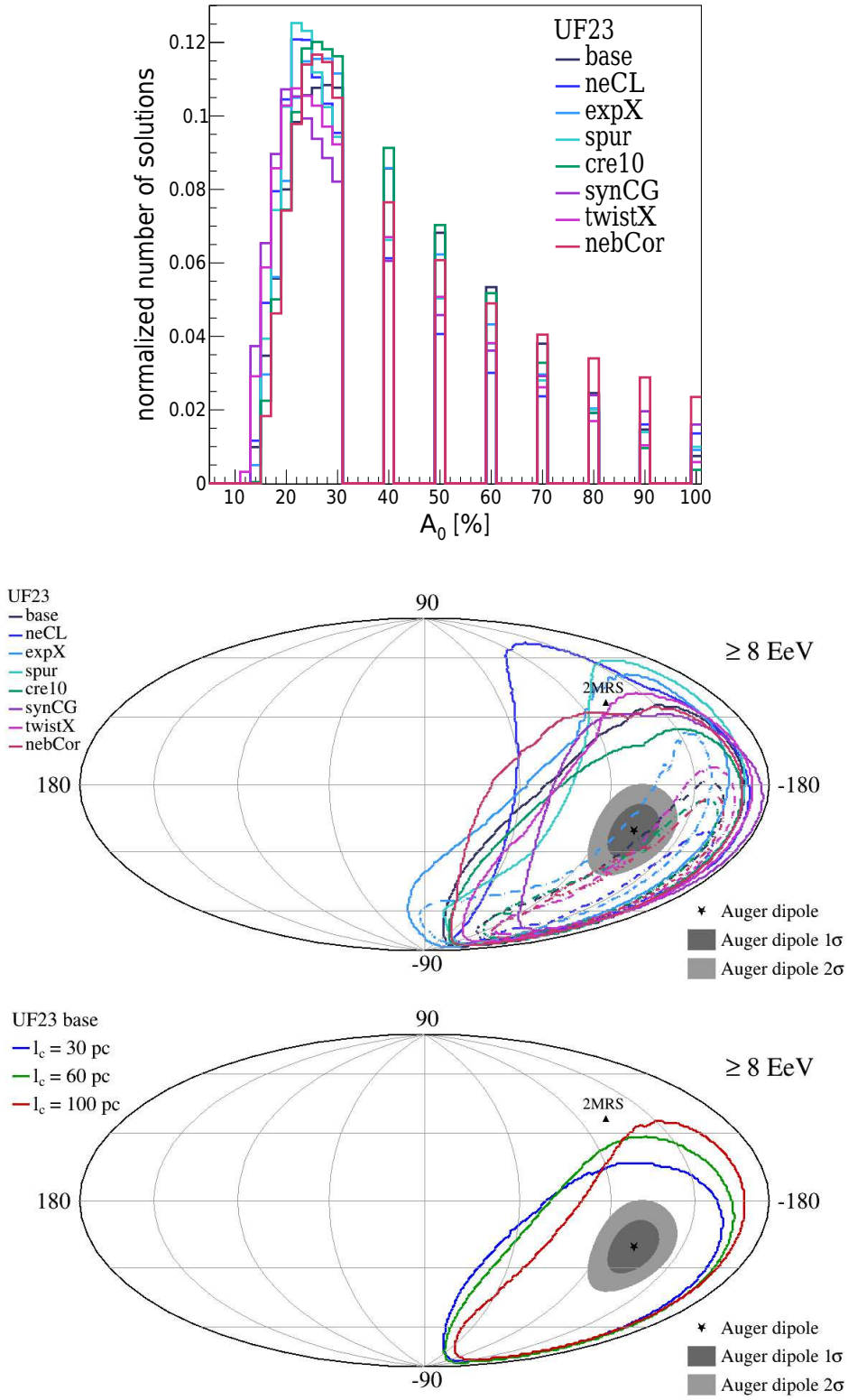

Figure 9. Top panel: the normalized distribution of the extragalactic amplitudes of the identified solutions from the top panel of Figure 5 for the individual models of the UF23 model of the GMF. Middle panel: possible extragalactic directions of a dipole, compatible at the 1σ (dashed lines) and 2σ (solid lines) levels with the Auger measurement for the eight individual UF23 models of the GMF, shown in Galactic coordinates, using the mass composition obtained for model SIBYLL 2.3d + $\Delta X_{\rm max}$. Bottom panel: possible extragalactic directions of a dipole at the 2σ level for the UF23 base model of the GMF and three different coherence lengths, shown in Galactic coordinates, using the mass composition obtained for the model SIBYLL 2.3d + $\Delta X_{\rm max}$.

as the 100 most energetic events seen by the Pierre Auger Observatory (A. Abdul Halim et al. 2023a). The geometrical exposure of the Pierre Auger Observatory is taken into account. The sky map shows similar features to the case of backtracking the real arrival directions of the 100 most energetic events, indicating that under the assumption of pure

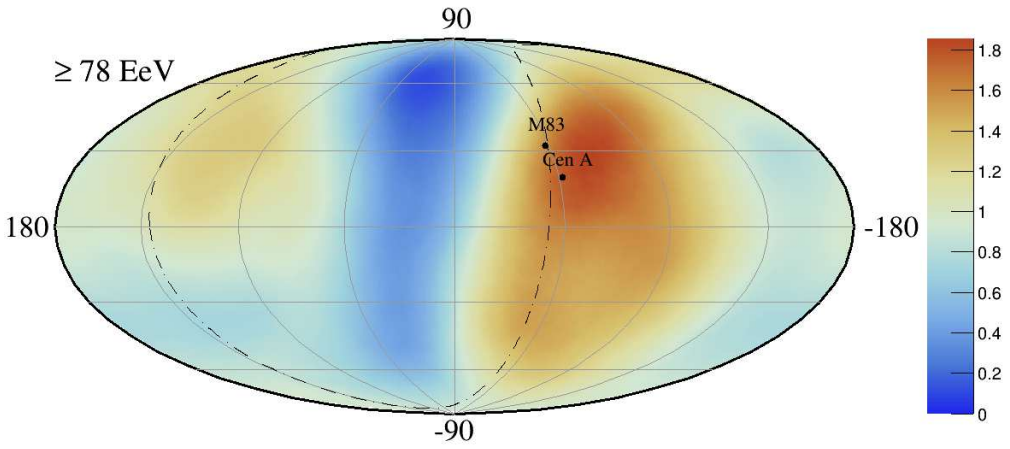

Figure 10. The ratio of the 100 most energetic backtracked Auger events to the expectation for backtracked isotropically distributed arrival directions on Earth, smoothed with a 25° top-hat function, shown in Galactic coordinates. The supergalactic plane is depicted by dashed–dotted lines with indicated directions of selected groups of galaxies.

iron nuclei, most of the particles are coming from the Galactic anticenter region.

ORCID iDs

Jakub Vícha https://orcid.org/0000-0002-7945-3605
Alena Bakalová https://orcid.org/0000-0003-1001-4484
Ana L. Müller https://orcid.org/0000-0002-8473-695X
Olena Tkachenko https://orcid.org/0000-0001-6393-7851
Maximilian K. Stadelmaier https://orcid.org/0000-0002-7943-6012

References

Aab, A., Abreu, P., Aglietta, M., et al. 2014a, PhRvD, 90, 122005
Aab, A., Abreu, P., Aglietta, M., et al. 2014b, PhRvD, 90, 122006
Aab, A., Abreu, P., Aglietta, M., et al. 2015a, NIMPA, 798, 172
Aab, A., Abreu, P., Aglietta, M., et al. 2015b, PhRvD, 91, 032003
Aab, A., Abreu, P., Aglietta, M., et al. 2016a, PhRvL, 117, 192001
Aab, A., Abreu, P., Aglietta, M., et al. 2016b, PhLB, 762, 288
Aab, A., Abreu, P., Aglietta, M., et al. 2017, Sci, 357, 1266
Aab, A., Abreu, P., Aglietta, M., et al. 2017a, JCAP, 04, 038
Aab, A., Abreu, P., Aglietta, M., et al. 2017b, PhRvD, 96, 122003
Aab, A., Abreu, P., Aglietta, M., et al. 2020a, EPJC, 210, 751
Aab, A., Abreu, P., Aglietta, M., et al. 2020b, PhRvD, 102, 062005
Aab, A., Abreu, P., Aglietta, M., et al. 2020c, PhRvL, 125, 121106
Aab, A., Abreu, P., Aglietta, M., et al. 2021, PhRvL, 126, 152002
Abbasi, R. U., Abe, Y., Abu-Zayyad, et al. 2024, PhRvL, 133, 041001
Abbasi, R. U., Allen, M. G., Arimura, R., et al. 2023, Sci, 382, 903
Abdul Halim, A., Abreu, P., Aglietta, M., et al. 2023, ApJS, 264, 50
Abdul Halim, A., Abreu, P., Aglietta, M., et al. 2024a, PhRvD, 109, 102001
Abdul Halim, A., Abreu, P., Aglietta, M., et al. 2024b, ApJ, 976, 48
Abdul Halim, A., Abreu, P., Aglietta, M., et al. 2025a, PhRvL, 134, 021001
Abdul Halim, A., Abreu, P., Aglietta, M., et al. 2025b, PhRvD, 111, 022003
Abreu, P., Aglietta, M., Ahlers, M., et al. 2013, JCAP, 02, 026
Abreu, P., Aglietta, M., Ahn, E. J., et al. 2012, PhRvL, 109, 062002
Abu-Zayyad, T., Aida, R., Allen, M., et al. 2012, NIMPA, 689, 87
Adam, R., Ade, P. A. R., Alves, M. I. R., et al. 2016, A&A, 596, A103
Albrecht, J., Cazon, L., Dembinski, H., et al. 2022, Ap&SS, 367, 27
Allard, D., Parizot, E., Olinto, A. V., Khan, E., & Goriely, S. 2005, A&A, 443, L29
Alves Batista, R., Becker Tjus, J., Dörner, J., et al. 2022, JCAP, 09, 035
Bakalová, A., Vícha, J., & Trávníček, P. 2023, JCAP, 12, 016
Bergmann, T., Engel, R., Heck, D., et al. 2007, APh, 26, 063002
Bister, T., Farrar, G. R., & Unger, M. 2024, ApJL, 975, L21
Ding, C., Globus, N., & Farrar, G. R. 2021, ApJL, 913, L13
Ebr, J., Blazek, J., Vìcha, J., et al. 2023, ICRC (Nagoya), 444, 245
Erdoğdu, P., Huchra, J. P., Lahav, O., et al. 2006, MNRAS, 368, 1515
Farrar, G. R. 2025, PhRvL, 134, 081003
Fitoussi, T. 2023, ICRC (Nagoya), 444, 319
Gilmore, R. C., Somerville, R. S., Primack, J. R., & Domínguez, A. 2012, MNRAS, 422, 3189
Harari, D., Mollerach, S., & Roulet, E. 2015, PhRvD, 92, 063014
Jansson, R., & Farrar, G. R. 2012, ApJ, 757, 14
Jiang, Y., Zhang, B. T., & Murase, K. 2021, PhRvD, 104, 043017
Komossa, S., & Mathur, S. 2001, A&A, 374, 914
Liu, A., Tozzi, P., Ettori, S., et al. 2020, A&A, 637, A58
Metzger, B. D., Giannios, D., & Horiuchi, S. 2011, MNRAS, 415, 2495
Murase, K., & Fukugita, M. 2019, PhRvD, 99, 063012
Ostapchenko, S. 2011, PhRvD, 83, 014018
Ostapchenko, S. 2024, PhRvD, 109, 094019
Pierog, T., Karpenko, I., Katzy, J. M., Yatsenko, E., & Werner, K. 2015, PhRvC, 92, 034906
Pierog, T., & Werner, K. 2023, ICRC (Nagoya), 444, 230
Riehn, F., Engel, R., Fedynitch, A., Gaisser, T. K., & Stanev, T. 2020, PhRvD, 102, 063002
Sommers, P. 2001, APh, 14, 271
Stadelmaier, M., Engel, R., Roth, M., Schmidt, D., & Veberič, D. 2024, PhRvD, 110, 023030
Stadelmaier, M. 2023, ICRC (Nagoya), 444, 339
Tkachenko, O., Engel, R., Ulrich, R., & Unger, M. 2021, ICRC (Berlin), 395, 438
Todero Peixoto, C. J. 2019, ICRC (Madison, WI), 358, 440
Unger, M., & Farrar, G. R. 2024, ApJL, 962, L5
Unger, M., & Farrar, G. R. 2024, ApJ, 970, 95
Vícha, J., Bakalová, A., Tkachenko, O., Laura Müller, A., & Stadelmaier, M. 2025, in Proc. of 7th Int. Symp. on Ultra High Energy Cosmic Rays—PoS (UHECR2024), 484, 123, https://pos.sissa.it/cgi-bin/reader/conf.cgi?confid=484
Werner, N., Böhringer, H., Kaastra, J. S., et al. 2006, A&A, 459, 353
Yushkov, A. 2019, ICRC (Madison, WI), 358, 482
Zhang, B. T., Murase, K., Ekanger, N., Bhattacharya, M., & Horiuchi, S. 2024, arXiv:2405.17409